RESEARCH ARTICLE | JULY 25 2019

CFD numerical model for open volumetric receivers with graded porosity dense wire meshes and experimental validation

Antonio L. Avila-Marin ✉; Jesús Fernandez-Reche; Cyril Caliot; Adela Martinez-Tarifa; Monica Alvarez de Lara

AIP Conf. Proc. 2126, 030005 (2019)
https://doi.org/10.1063/1.5117517

CFD Numerical Model for Open Volumetric Receivers with Graded Porosity Dense Wire Meshes and Experimental Validation

Antonio L. Avila-Marin[1, a)], Jesús Fernandez-Reche[2], Cyril Caliot[3], Adela Martinez-Tarifa[1], and Monica Alvarez de Lara[4]

[1]*CIEMAT – Plataforma Solar de Almeria (PSA); Avda. Complutense 40, Madrid E-28040, Spain*
[2]*CIEMAT – Plataforma Solar de Almeria (PSA); P.O. Box 22, Tabernas-Almeria E-04200, Spain*
[3]*PROMES CNRS, 7 Rue du Four Solaire, 66120 Font-Romeu, France*
[4]*MINECO, Paseo de la Castellana 162, Madrid E-28046, Spain*

[a)]Corresponding author: antonio.avila@ciemat.es

Abstract. This paper presents a numerical methodology with homogenized equations, together with the main assumptions and boundary conditions to analyze the thermal performance of open volumetric receiver with dense wire meshes and graded porosity. Main numerical results of double and triple porosity absorbers are presented, together with a comparison of the numerical results with experimental data showing a good agreement. The analysis of the results concluded that double porosity absorbers gets the best performance when the rear meshes has a high specific surface area and, triple porosity absorbers are not able to improve on the best case of double porosity absorbers. However, the graded concept has demonstrated to have the potential to improve the performance of single porosity absorbers.

INTRODUCTION

Central Receiver Systems (CRS) using Open Volumetric Receiver (OVR) technology is receiving a renovated interest because of its potential to increase the solar to electrical efficiency in solar power tower plants [1] and the associated advantages of the air receiver (such as availability of the fluid, no trace heating necessary, non-toxic, and 3–5 h of thermal storage) [2-5]. This technology has the potential to increase the Heat Transfer Fluid (HTF) temperature, reduce the thermal losses and, use high efficiency thermodynamic cycles. Since high efficiencies in the thermodynamic cycles are related to high HTF working temperatures, the most investigated option previously studied is the ceramic materials [6-8]. Several studies have been done to predict the thermal behavior of ceramic porous media. Pitz-Paal et al. [9] analyzed the thermal performance and flow instability of a OVR with a three-dimensional irradiance distribution. Wu et al. [10] analyzed in a macroscopic CFD model several geometric and operating parameters using a local thermal non-equilibrium (LTNE) model coupled to the P_1-approximation. Fend et al. [11] modeled both a single-channel and a cup of a honeycomb absorber, showing that the finer geometry performed better. Kribus et al. [12] investigated in a uni-dimensional (1-D) model the performance of OVR as function of geometrical and material properties giving emphasis on the implementation of the radiative heat transfer. Recently, Zaversky et al. [8] presented two 1-D models with different characteristics using both LTNE validated against experimental data and performing parametric optimization over geometrical foam parameters. Large experimental and numerical work has been performed over the OVR performance, mainly focused on ceramic materials.

On the other hand, metallic materials have not received such interest, despite their advantages: the opportunity to easily work with different configurations, lightweight structures, lower working temperatures than ceramic materials, etc. [13-14]. Recently, Livshits et al. [15] proposed volumetric structures made of dense metallic plain-weave wire mesh screens as an interesting candidate to reach absorber efficiencies exceeding 90% and, Avila-Marin et al. [13-16]

SolarPACES 2018
AIP Conf. Proc. 2126, 030005-1–030005-8; https://doi.org/10.1063/1.5117517
Published by AIP Publishing. 978-0-7354-1866-0/$30.00

numerically studied the convective HTC for six commercially available mesh types and different stack patterns, and the correlations were validated against experimental and numerical results.

This paper presents a numerical study of OVR made with graded dense metallic screens, coupling heat transfer and fluid flow with homogenized equations, assuming local thermal non-equilibrium and adopting P_1 model as the radiative transfer model. Finally, the numerical model is validated against experimental data.

SOLAR ABSORBER DESCRIPTION

The solar absorber studied in this work consists of a cylindrical pipe that contains different dense wire mesh stacked. The absorbers that are going to be numerically analyzed are those experimentally studied in Avila-Marin [14, 17, 18] who has exhaustively studied gradual porosity absorbers.

For the CFD simulations, 6 commercial square plain-weave wire mesh screens with a diameter of 50 mm are used. Table 1 presents the main properties for the 6 screens adopted in this work [13, 14], where d is the wire diameter, M is the mesh count or mesh number, $\emptyset$ is the porosity, a_v is the specific surface area and is the extinction coefficient (calculated by means of geometrical optics [19]). The thickness of each absorber analyzed in this paper was selected experimentally according to a thickness that ensures the total extinction of the incident flux profile in the whole absorber volume. The number of screens used for the graded absorbers is presented in [14].

TABLE 1. Commercial AISI 310 square plain-weave wire mesh characteristics

Mesh type			A	C	D	E	F
Mesh properties	d	mm	1.00	0.50	0.16	0.63	0.13
	M	mm^{-1}	0.20	0.53	1.79	0.61	3.03
	$\emptyset$	%	70.1	62.0	61.8	47.7	46.9
	a_v	m^{-1}	1194	3044	9552	3322	16330
	β	m^{-1}	760	1938	6081	2115	10396

MATHEMATICAL MODEL

The numerical model of the combined flow and heat transfer in the solar receiver is based on several assumptions: (a) the fluid (air) is Newtonian and behaves like an ideal gas; (b) the fluid flow is at steady state and laminar, because the maximum Reynolds number (based on the hydraulic diameter and superficial velocity), was lower than 200; (c) the physical properties of the fluid phase are variable due to the large variation during the simulations; (d) the physical properties of the dense wire mesh stack are temperature dependent; (e) the porous formed by dense wire mesh is considered gray, absorbing, emitting and scattering is isotropic; (f) lateral walls of solar absorber are adiabatic. The governing equations are presented:

Governing Equations

Momentum equation:

The flow in porous media can be described by the Brinkman-Forchheimer extended Darcy model [20]:

$$\frac{\rho_f}{\emptyset}\langle(v_D\cdot\nabla)\rangle\, v_D = -\nabla\langle P_f\rangle^f + \frac{\mu_f}{\emptyset}\nabla^2\langle v_D\rangle - \frac{\mu_f}{K_1}\langle v_D\rangle - \frac{\emptyset\cdot\rho_f}{K_2}[\langle v_D\rangle\cdot\langle v_D\rangle] \quad (1)$$

Where μ_f is the fluid dynamic viscosity, $\emptyset$ is the porosity, P_f is the fluid pressure, K_1 is the inertial permeability coefficient, K_2 is the viscous permeability coefficient and v_D is the Darcy velocity.

Energy equations:

This model considers the local thermal non-equilibrium (LTNE) between the fluid and the solid phases, which accounts a difference between the air and porous matrix temperatures. The two equations are linked by the convective source term, using the effective property called the volumetric convective Heat Transfer Coefficient (HTC), h_v.

- For the fluid phase:

$$\left(\rho_f c_f\right) \langle v_D \rangle \cdot \nabla \langle T_f \rangle = \nabla\left(k_{eff,f} \cdot \nabla \langle T_f \rangle\right) + h_v \left(\langle T_s \rangle - \langle T_f \rangle\right) \quad (2)$$

- For the porous phase:

$$0 = \nabla \cdot \left(k_{eff,s} \cdot \nabla \langle T_s \rangle - q_r\right) + h_v \cdot \left(\langle T_f \rangle - \langle T_s \rangle\right) \quad (3)$$

Among the two equations, T_f and T_s represents the temperature of the fluid and the porous phases and, $k_{eff,f}$ and $k_{eff,s}$ mean the effective thermal conductivity of the fluid and the porous phases respectively. h_v is the volumetric convective HTC. q_r is the radiative heat flux source, ρ_f,c_f mean the density and heat capacity of the fluid and the symbols $\langle \ \rangle$ mean the volumetric average.

P_1-approximation equations:

The P_1-approximation is used in this study because it is suitable for optically thick media and it is not time consuming. The dense mesh screens was irradiated with a solar simulator which was assumed to be a collimated incident radiation beam, so, the P_1-model is used with the intensity splitting technique which uses collimated and diffuse intensities [21]. The transport equation of the diffuse integrated intensity, G_s is:

$$-\nabla \left(\Gamma \cdot \nabla G_s\right) = a \cdot \left(4 \cdot \sigma \cdot T_s^4 - G_s\right) + \sigma_s \cdot I_0 \cdot e^{-\beta \cdot z} \quad (4)$$

Where β is the extinction coefficient, a is the absorption coefficient, σ is the Stefan-Boltzmann constant and, z is the porous absorber thickness. Once the diffuse irradiation, G_s, is solved, the divergence of the radiative flux is computed:

$$\nabla q_r = a \cdot \left(4 \cdot \pi \cdot i_b - G_c - G_s\right) \quad (5)$$

Boundary Conditions

The following boundary conditions apply for the CFD simulations:

Concentrated solar incident flux:

The incoming concentrated solar incident flux is treated as parallel, constant and uniform with a value of 600 kW/m^2.

Inlet conditions:

- Fluid: The fluid velocity is set at 1 m/s and the static temperature is fixed to 300 K.
- Solid: The temperature gradient at the solid outlet surface is set to zero.
- P1-approximations: The same boundary sets in previous works [2, 10] is applied.

Outlet conditions:

- Fluid: The temperature gradient at the fluid outlet surface and the static pressure (with a reference pressure of 101325 Pa) are set to zero.
- Solid: The temperature gradient at the solid outlet surface is set to zero.
- P1-approximations: The incident irradiation gradient at the outlet surface is set to zero.

Coefficients for the CFD Model

This study simulates the temperature distribution of the fluid and solid phases by solving the coupled volume-averaged governing equations reducing computational time compared to pore-scale studies. Thus, it needs several effective properties for an accurate solution of the model, as the ones presented in Table 2. The main coefficients have been adopted from literature data [13, 14, 17].

TABLE 2. Coefficients needed for the homogenous equivalent model

Equation	Variable	Description	Units
Momentum	K_1	Viscous permeability coefficient	m^2
	K_2	Inertial permeability coefficient	m
	∅	Porosity	-
Energy	h_{lv}	Local volumetric heat transfer coefficient	$W/(m^3 \cdot K)$
	$k_{eff,f}$	Fluid effective conductivity	$W/(m \cdot K)$
	$k_{eff,s}$	Solid effective conductivity	$W/(m \cdot K)$
Radiative	a	Absorption coefficient	m^{-1}
	σ_s	Scattering coefficient	m^{-1}
	β	Extinction coefficient	m^{-1}

Numerical Method

Various absorbers with double and triple graded porosities made of dense wire mesh are studied using the commercial CFD code, STAR-CCM+8.04.010® with user defined functions. The simulations were performed under a constant incident flux of 600 kW/m^2 and a fluid inlet velocity of 7 m^3/h. The physical model consists on a simple cylindrical pipe with different thicknesses depending on the absorber analyzed [14]. The user functions are coupled with STAR-CCM+ solver for enhancing the standard features [22]. The user defined functions are used to define boundary conditions, material and fluid properties and source terms. For the LTNE model, the additional scalar equation and source terms in the solid energy equations are solved through Passive Scalars and user-defined-functions. The velocity and the pressure coupling are handled with SIMPLE algorithm. The momentum equation, the energy equations and P_1-approximation are discretized by adopting the second-order upwind model. The set of governing equations is solved in a segregated way, which means that the discretized momentum, energy and passive scalar equations are solved one by one during the iterations.

RESULTS AND DISCUSSION

This works continues with the experimental analysis already presented in Avila-Marin [14] with dense wire mesh. For the experimental work, six commercial metallic plain-weave wire mesh screens were selected with different geometric characteristics, but with the constraint of finding pairs with similar porosities (see Table 1). Within the experimental work, with the aforementioned meshes, 26 volumetric absorbers -6 with single porosity, 12 with double porosity and 8 with triple porosity- were analyzed.

The following section focus on the numerical analysis of double and triple porosity absorbers with mesh type A as base. This means that the first porosity of the graded absorbers will be type A mesh. For the double porosity absorbers, the base mesh is combined with those meshes that have lower volumetric porosity (see Table 1), so, the base-mesh type A is used to construct four double porosity absorbers (AC, AD, AE, AF). And, the triple porosity absorbers are based on the double porosity designs AC and AD, to which are added meshes of lower porosity according to the following plan: high porosity/average porosity/low porosity. The thickness of the layers are presented in Avila-Marin et al. [14].

Double Porosity with Base Mesh Type A

This section compares four absorbers with double porosity using mesh type A as base (or as first porosity). Figure 1 depicts the solid and fluid temperature profiles as function of the absorber relative position for the absorbers AC, AD, AE and AF and, Table 3 present a summary of the main results. The analysis of the results shows that:

- All the double porosity absorbers with base mesh A improve on the performance of the absorber with single porosity with mesh type A.

- The greatest improvement is produced by configuration AF, which produces the highest air outlet temperatures.
- The remainders of the absorber combinations have decreasing efficiencies depending on the specific surface (Table 1) area of the mesh located behind the base mesh A.

Once the first porosity is selected (mesh type A), the best choice is to have as the second porosity of the absorber the one with the highest specific surface area possible, as happens with configuration AF. The reason is that the HTC is increasing with the specific surface area of the second layer, causing a better HTC.

Furthermore, the configuration AF combines the most extreme meshes of this study (Table 1). On one hand, base mesh type A with the lowest specific surface area and extinction coefficient, allowing the highest solar penetrability toward the inside of the receiver, while the second porosity (located in the back part of the absorber), mesh type F, present the opposite properties and, is the responsible of the improvement of the heat transfer between the mesh and the air of the radiation transmitted by type A mesh. Moreover, for these combinations of absorbers (AC, AD, AE, AF), the specific surface area of the mesh located at the back determine the overall performance of the configuration. The higher the specific surface area of the mesh located at the back is the higher thermal efficiency of the absorber.

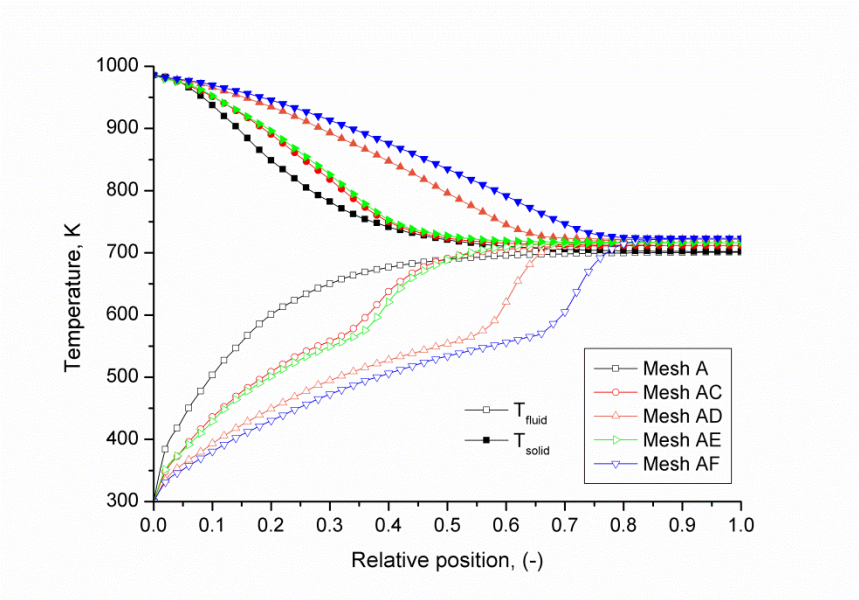

FIGURE 1. Solid and fluid temperature profiles for the double porosity absorbers: AC-AD-AE-AF

Triple Porosity with Base Mesh Type A

This section compares four absorbers with triple porosity using mesh type A as base (or as first porosity). Figure 2 depicts the solid and fluid temperature profiles as function of the absorber relative position for the triple porosity absorbers ACE, ACF, ADE, and ADF and, Table 3 present a summary of the main results. The analysis of the results shows that:

- All the triple porosity absorbers improved on the behavior of the single porosity absorber with mesh type A.
- The triple porosity designs based on the AC configuration match or slightly improve on the AC base absorber, while just one triple porosity design (ADF) based on the AD configuration improve the AD base absorber slightly and the remaining (ADE) get a slightly poorer result.
- Among all the triple porosity designs, the absorbers that show the best results are the ADF and ADE configurations, in that order.
- The two pairs of triple porosity configurations, ACE-ACF and ADE-ADF have very similar performance both between the members of the pairs and with their respective double porosity configurations of AC and AD.

From the previous results, it can be concluded that:

- The last porosity of the triple porosity absorbers has only a slight benefit on the performance. This benefit is higher when the second porosity has as high specific surface area as possible, as more heat is transferred toward the third porosity.
- The configurations that perform better are those that have a porosity that decreases with the thickness of the volumetric absorber. Moreover, its behavior is improved when the specific surface area has a value that increases with the thickness, especially in the average porosity region.
- The efficiency of the absorber improves when the last mesh of each composition is of type F. Even so, the improvement that is produced with respect to the AC and AD double porosity absorbers is very slight.
- Overall, none of the triple porosity absorbers are able to match or improve on the behavior of the best double porosity absorber (AF). Only the triple configuration ADF (87.0%) get a slightly worse performance than AF (87.1%), and its performance is in-between the double porosity absorber AD (86.7%) and AF (87.1%).

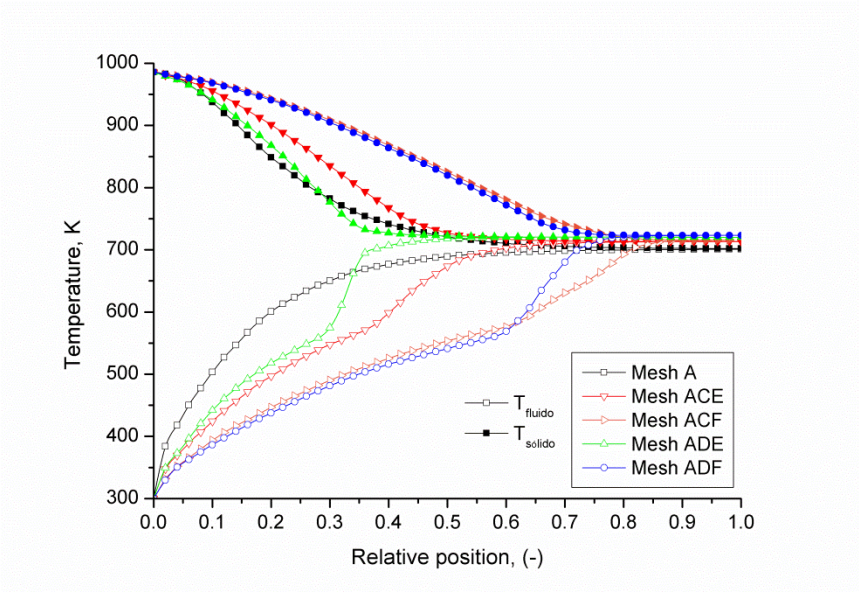

FIGURE 2. Solid and fluid temperature profiles for the triple porosity absorbers: ACE-ACF-ADE-ADF

TABLE 3. Summary of the main results for the double and triple porosity absorbers with base mesh type A

Mesh		A	AC	AD	AE	AF	ACE	ACF	ADE	ADF
ø	%	70	70/62	70/62	70/48	70/47	70/62/48	70/62/47	70/62/48	70/62/47
$T_{f\text{-}out}$	K	701.0	711.6	721.5	716.2	723.3	713.3	715.5	719.6	722.5
η_{abs}	%	82.4	84.6	86.7	85.6	87.1	85.0	85.5	86.3	87.0

Model Validation

This section presents the validation of a dense wire pack mesh carried out at lab scale under a non-homogeneous concentrated radiation [14]. The experimental tests were performed with similar incident radiation, with different mass flow rates and each test was repeated at least three times. The mean results of the tests carried out are presented together with the results of the numerical model adapted to the experimental working conditions.

Table 4 presents the experimental results of the double porosity OVR made of metallic wire meshes together with the numerical (N) results of the adapted model and the deviation (D) between both results for an air inlet velocity of 1 m/s.

The results show a good agreement in terms of fluid temperature between the experimental and numerical results with a maximum deviation of nearly 1.2 %.

TABLE 4. Experimental (E) and numerical (N) air averaged outlet temperature and deviation (D) results for double porosity OVR at 1 m/s

Configuration	E, (K)	N, (K)	D, (%)
AC	597	595	-0.3
AD	602	599	-0.5
AE	598	597	-0.1
AF	606	599	-1.2

CONCLUSIONS

This work presents a numerical study of OVR made with dense metallic screens, coupling heat transfer and fluid flow with homogenized equations, assuming local thermal non-equilibrium and adopting P_1 model as the radiative transfer model.

The numerical analysis of graded porosity OVR shows that the concept has been demonstrated to have potential, in absence of an optimization process, which can improve, or at least match, the efficiency of single porosity absorbers.

From the results it is concluded that:

- Double porosity configurations behave better when the rear meshes has as high specific surface area as possible.
- Triple porosity configurations: 1) are not able to improve on the best double porosity configuration and, 2) achieve its best behavior when the specific surface area has a value that increases with the thickness, especially in the average porosity region.

Finally, the experimental results of four double porosity configurations are compared with the numerical results by means of the mean temperature of the fluid at the absorber outlet. The comparison shows a maximum deviation of 1.2%, so the numerical model is considered validated.

ACKNOWLEDGEMENTS

The author wish to thank “Comunidad de Madrid” and “European Social Fund” for its financial support to the ALCCONES project through the Programme of Activities between Research Groups (S2013/MAE-2985) and to the “DETECSOL” project funded by the Spanish government with ERDF funds with reference ENE2014-56079-R.

REFERENCES

1. X. Chen, X.-L. Xia, H. Liu, Y. Li, B. Liu, Energy Conversion and Management, **114**, 20-27 (2016).
2. X. Chen, X.-L. Xia, X.-L. Meng, X.-H. Dong, Energy Conversion and Management, **97**, 282-289 (2015).
3. M. Romero, R. Buck, J.E. Pacheco, Solar Energy Engineering, **124**, 98-108 (2002).
4. J.-F.P. Pitot de la Beaujardiere, H.C.R. Reuter, S.A. Klein, D.T. Reindl, Solar Energy, **127**, 159-174 (2016).
5. A.L. Avila-Marin, M. Alvarez-Lara, J. Fernandez-Reche, Energy Procedia, **49**, 705-714 (2014).
6. M. Cagnoli, L. Savoldi, R. Zanino, F. Zaversky, Solar Energy, **155**, 523-536 (2017).
7. S. Mey-Cloutier, C. Caliot, A. Kribus, Y. Gray, G. Flamant, Solar Energy, **136**, 226-235 (2016).
8. F. Zaversky, L. Aldaz, M. Sánchez, A.L. Avila-Marin, M.I. Roldán, J. Fernández-Reche, A. Füssel, W. Beckert, J. Adler, Applied Energy, **210**, 351-375 (2018)
9. R. Pitz-Paal, B. Hoffschmidt, M. Böhmer, M. Becker, Solar Energy, **60**, 135-150 (1997).
10. Z. Wu, C. Caliot, G. Flamant, Z. Wang, Solar Energy, **85**, 2374-2385 (2011).
11. T. Fend, P. Schwarzbözl, O. Smirnova, D. Schöllgen, C. Jakob, Renewable Energy, **60**, 655-661 (2013).
12. A. Kribus, Y. Gray, M. Grijnevich, G. Mittelman, S. Mey-Cloutier, C. Caliot, Solar Energy, **110**, 463-48, (2014).

13. A.L. Avila-Marin, C. Caliot, G. Flamant, M. Alvarez de Lara, J. Fernandez-Reche, Solar Energy, **162**, 317-329 (2018).
14. A.L. Avila-Marin, M. Alvarez de Lara, J. Fernandez-Reche, Renewable Energy, **122**, 339-353 (2018).
15. M. Livshits, L. Avivi, A. Kribus, "Dense wire mesh as a high-efficiency solar volumetric absorber", in ASME Summer Heat Transfer Conference, Bellevue, Washington, USA, paper HT-2017-5080 (2017).
16. A.L. Avila-Marin, J. Fernandez-Reche, M. Casanova, C. Caliot, G. Flamant, AIP Conference Proceedings 1850, 030003 (2017).
17. A.L. Avila-Marin, "Análisis termofluidodinámico de absorbedores volumétricos de porosidad gradual con mallas metálicas: Estudio experimental a escala de laboratorio y desarrollo de un modelo de no equilibrio térmico local". Dissertation. Ingeniería Energética. Madrid. ETSII - UNED (2016).
18. A.L. Avila-Marin, M. Alvarez-Lara, J. Fernandez-Reche, Energy Procedia, **49**, 275-283 (2014).
19. K. Vafai, Handbook of porous media, Third Edition. Taylor & Francis Group. CRC Press (2015).
20. P. Wang, K. Vafai, D.Y. Liu, Numerical Heat Transfer, Part A: Applications, **65**, 931-948 (2014).
21. M.F. Modest, Radiative Heat Transfer, Second ed. McGraw-Hill, New York (2003).
22. STAR-CCM+, Version 8.04.010, User Guide, CD-adapco, http://cd-adapco.com (2015).